THREE-DIMENSIONAL VISCOUS FLOW SIMULATIONS OVER A COMPLETE SATELLITE LAUNCHER USING OVERSET GRIDS

Edson Basso and João Luiz F. Azevedo
CTA/IAE/ASE-N12228-904 – São José dos Campos – SP – BRAZIL

Keywords: *Viscous simulations, Chimera grids, Finite difference method, Satellite launcher*

Abstract

This work is inserted in the effort to develop a Chimera flow simulation code capable of handling general launch vehicle configurations. The work presents aerodynamic results referring to laminar and turbulent viscous simulations over the first Brazilian satellite launch vehicle, VLS, during its first-stage flight. The finite difference method is applied to the governing equations written in conservation-law form for general body conforming curvilinear coordinates. The spatial discretization is accomplished with a central difference scheme in which artificial dissipation terms, based on a scalar, non-isotropic model, are added to the numerical scheme to maintain stability. The time march process is accomplished with a 5-stage, 2nd-order accurate, Runge-Kutta scheme. Studies of mesh refinement are also presented as a part of the validation effort, which has the objective of providing a certified flow simulation capability for actual engineering work.

1 Introduction

In the present work, laminar and turbulent viscous simulations are accomplished with the objective of reproducing the aerodynamic phenomena that are present during the first stage flight of the first Brazilian satellite launch vehicle, VLS. The basic motivation for this work is to provide a continuation in the development effort that has been going on in the institutions here represented, which aims at creating the simulation capability to handle truly complex aerospace configurations. In particular, there is strong interest in performing simulations over the VLS first-stage flight configuration, since this is a fairly complex vehicle with several bodies in close proximity. Three-dimensional results for this complete configuration were already obtained with the Euler formulation using the previous version of the Chimera flow simulation code under consideration here. These results are described in detail in Ref. [1], together with a historical perspective of the development of CFD tools for flow simulation over general launch vehicle configurations at these institutions. The inviscid calculations were not able to obtain good correlation with the experimental data over some portions of the vehicle, regardless of the level of mesh refinement. Furthermore, at the time, there was some evidence that viscous effects could dominate the flow in these regions. In particular, over the region in which there is close proximity between the VLS central body and its strap-on boosters, it was not possible to obtain good comparisons between computational and experimental results with the inviscid solutions.

The flight configuration of the first stage of the VLS is composed by a central body and four strap-on boosters arranged symmetrically around this central body, as it can be observed in Fig. 1. This is, therefore, a quite complex geometry over which to generate a structured mesh. Hence, there has been an effort to develop tools based on the overset, multiblock grid technique, or Chimera [2, 3], in order to simulate flows over the complete VLS vehicle.

This technique provides the capability to use structured meshes for the discretization of the calculation domain over truly complex configurations. Moreover, it allows adaptive grid refinement characteristics, which are similar to those, achieved with unstructured meshes, although such capability will not be exploited in the context of the present paper. The governing equations are assumed written in conservative form and these equations are discretized by a finite difference method. Spatial discretization uses second-order accurate, central difference operators. The time march method is based on a 5-stage, Runge-Kutta algorithm [4], which also has second-order accuracy in time. The artificial dissipation terms added are based on the non-isotropic, Turkel and Vatsa model [5].

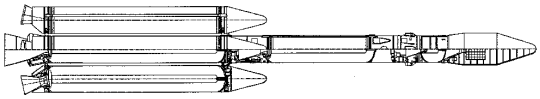

Figure 1: Schematic representation of the VLS system during its first-stage flight.

The effort here described implemented viscous terms in the context of the Chimera code already available [1] in order to perform the present studies. Moreover, since actual flight conditions over the VLS and similar vehicles consider Reynolds numbers, which typically are in the order of tens of millions, or higher, the present work also provided an initial implementation of an algebraic eddy viscosity model. So far, only the Baldwin and Lomax model [6] has been implemented and tested in the code. However, there are plans to extend the tests with this and other models in the future. Furthermore, in order to perform viscous numerical simulations, it is necessary to generate grids, which are fine enough to provide support for capturing viscous effects throughout the flowfield. In the present case, since the afterbody body portion of the vehicles is not included in the simulations, it is correct to state that viscous effects will be restricted to fairly thin boundary layers. Hence, in the interest of computational efficiency, grid refinement is particularly emphasized in the wall-normal direction and the simulations here presented should be considered as solutions of the thin-layer Navier-Stokes equations, despite the fact that more viscous terms are included in the equations actually implemented in the code.

The forthcoming sections will present the governing equations together with some details of the numerical method used for their solution. A brief discussion of the boundary conditions implemented is also presented, as well as an overview of the Chimera grid procedure used in the present code. Viscous laminar and turbulent solutions for the complete VLS vehicle are presented and discussed. The paper concludes with a critical evaluation of the flow simulation capability implemented and a discussion of perspectives for future work.

2 Governing Equation

It is assumed that the flows of interest in the present work can be represented by the Navier-Stokes equations in three dimensions. These equations can be written in conservation-law form for a curvilinear coordinate system as

$$\frac{\partial \overline{Q}}{\partial \tau}+\frac{\partial}{\partial \xi}\left(\overline{E}-\overline{E}_v\right)+\frac{\partial}{\partial \eta}\left(\overline{F}-\overline{F}_v\right)+\frac{\partial}{\partial \varsigma}\left(\overline{G}-\overline{G}_v\right)=0 \quad (1)$$

where $\overline{Q}$ is the vector of conserved variables, defined as

$$\overline{Q}=J^{-1}\left[\rho,\rho u,\rho v,\rho w,e\right]^T \quad (2)$$

In these equations, ρ is the density, *u*, *v* and *w* are the Cartesian velocity components and *e* is the total energy per unit of volume. The $\overline{E},\overline{F},$ and $\overline{G}$ are the inviscid flux vectors, and $\overline{E}_v,\overline{F}_v,$ and $\overline{G}_v$ are the viscous flux vectors. The complete expressions for the inviscid flux vectors can be found Ref. [7], and expressions for the viscous flux vectors, as implemented here, can be found, for instance, in Ref. [8]. It is important to emphasized that, consistent with previous comments, the cross derivative terms were eliminated in the definition of the viscous

flux vectors actually implemented in the code. Expressions for the Jacobian of the transformation, J, as well as for the various metric terms can be found in Refs. [7] and [9], among other references. The pressure can be obtained from the equation of state for a perfect gas.

A suitable nondimensionalization of the governing equations has been assumed in order to write Eq. (1). In particular, the values of flow properties are made dimensionless with respect to freestream quantities, as described in Ref. [9].

The governing equations are discretized in a finite difference context on structured hexahedral meshes, which would conform to the bodies in the computational domain. Since a central difference spatial discretization method is being used, artificial dissipation terms must be added to the formulation in order to control nonlinear instabilities. The artificial dissipation terms used here are based on Turkel and Vatsa's scalar model [5]. This model is nonlinear and non-isotropic, with the scaling of the artificial dissipation operator in each coordinate direction weighted by its own spectral radius of the corresponding flux Jacobian matrix. The residue operator is defined as being the evaluation of the discretized partial differential equation (or system of partial differential equations) and, in this way, it represents how well the evaluation of the discretized form of the equations is being satisfied by the current solution, in the present iteration level *n*. The artificial dissipation terms are added to the residue operator to maintain nonlinear stability. In the present implementation, the residue operator is defined as

$$RHS_{i,j,k}^{(l)} = \Delta t_{i,j,k} \left\{ \delta_\xi \left(\bar{E}\right)_{i,j,k} - \bar{\delta}_\xi \left[\left(\bar{E}_v + J^{-1} d\right)_{i,j,k} \right] + \right.$$
$$+ \delta_\eta \left(\bar{F}\right)_{i,j,k} - \bar{\delta}_\eta \left(\bar{F}_v + J^{-1} d\right)_{i,j,k}$$
$$\left. + \delta_\varsigma \left(\bar{G}\right)_{i,j,k} - \bar{\delta}_\varsigma \left(\bar{G}_v + J^{-1} d\right)_{i,j,k} \right\} . \qquad (3)$$

Here, the δ_ξ, δ_η and δ_ς terms represent standard 3-point central difference operators in the ξ, η and ς directions, respectively. Similarly, $\bar{\delta}_\xi$, $\bar{\delta}_\eta$ and $\bar{\delta}_\varsigma$ are the mid-point central difference operators. The artificial dissipations operators, $d_{i\pm\frac{1}{2},j,k}$, $d_{i,j\pm\frac{1}{2},k}$ and $d_{i,j,k\pm\frac{1}{2}}$, which would appear from the application of the difference operators are defined precisely as described in Turkel and Vatsa's model [5].

Since steady state solutions are the major interest of the present study, a variable time step convergence acceleration procedure has been implemented.

The time march is performed based on a 5-stage, 2nd-order accurate, hybrid Runge-Kutta time-stepping scheme,

$$Q_i^{(0)} = Q_i^n ,$$
$$Q_i^{(l)} = Q_i^{(0)} - \alpha_l \, RHS^{(l-1)} \quad , l = 1,...,5 \quad , \qquad (4)$$
$$Q_i^{n+1} = Q_i^{(5)} .$$

Here, the α_l constants are defined as $\alpha_1 = \frac{1}{4}$, $\alpha_2 = \frac{1}{6}$, $\alpha_3 = \frac{3}{8}$, $\alpha_4 = \frac{1}{2}$, $\alpha_5 = 1$. It should be emphasized that only the convective operator inside the *RHS* term is actually evaluated at every time step. The viscous flux vectors are only evaluated at the first stage of the Runge-Kutta time-stepping scheme. Moreover, the artificial dissipation terms are evaluated at alternate stages, i.e., at the odd stages in the present case, of the time-march procedure. It can be shown that this provides enough damping to maintain nonlinear stability [4, 10], whereas it yields a more efficient numerical scheme.

Finally, turbulent simulations have used the Baldwin and Lomax [6] algebraic eddy viscosity model in order to provide turbulence closure. The turbulence model was implemented in this work in its standard form as described in the original paper by Baldwin and Lomax [6]. Since this model is very well known and its expressions are widely available, they will not be included here.

3 Results and Discussion

3.1 Laminar Viscous Simulations

The meshes used for the first viscous simulations of the flow over the complete VLS had 120 x 36 x 33 points in the ξ, η and ς directions, respectively, for each of the booster grids and 120 x 65 x 33 points for the central body. This grid is referred to here as the coarse grid. The actual complete configuration is used in the simulations, namely, the central body and four boosters are included in the definition of the computational domain. In these simulations, the freestream Mach number is assumed to be $M_\infty = 2.0$ and the angle of attack is zero. The Prandtl number is set to Pr = 0.72, and the Reynolds number is 10 million, based on the diameter of the central body of the vehicle. Figure 3 is a visualization of the Mach number contours in the longitudinal plane denominated "plane 1" in Fig. 2.

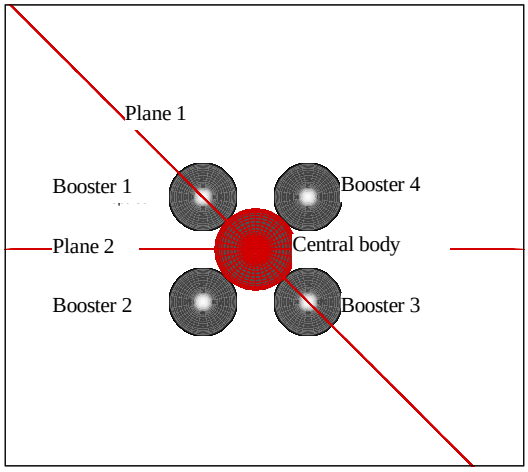

Figure 2: Top view of complete VLS configuration indicating some of the planes in which vehicle results are presented.

The boundary layer thickening along the central body surface, in the region immediately upstream of the lateral boosters, can be clearly seen in Fig. 3. The thickening of the boundary layer is initially a result of the detached bow shock, ahead of the boosters, impingement on the central body surface. The information on the pressure rise due to shock impingement propagates upstream through the boundary layer and, eventually, it causes flow separation upstream of the impingement point due to the weakening of the boundary layer momentum. Boundary layer separation, on the other hand, causes the creation of an oblique shock wave, which, unfortunately, is not clearly seen in Fig. 3. This oblique shock wave is more readily seen

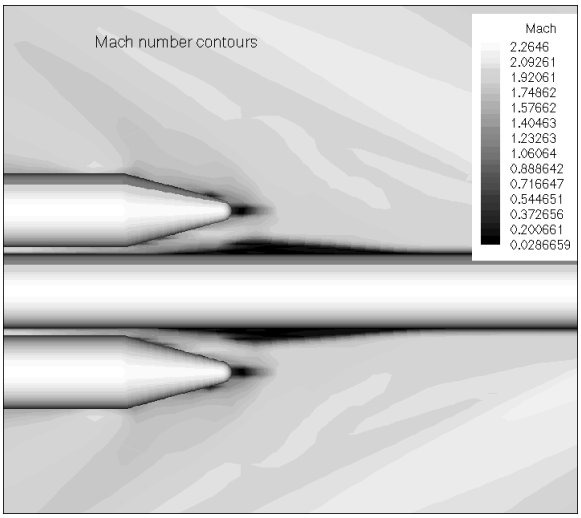

Figure 3: Mach number contours on plane 1 (Fig. 2) for laminar flow simulations with the coarse grid ($M_\infty = 2$, $\alpha = 0$ deg., Re = 10 million).

on pressure contour plots. It is important to point out that these flow features ahead of the booster nose caps are not present in the Euler simulations reported in Ref. [1]. This indicates that, even with coarse grids, the viscous solutions are providing flow structures, which are different from the ones seen in the Euler cases.

Figure 4 presents the velocity vectors on a flow plane, which contains the central body axis and the axes of two boosters (plane 1 in Fig. 2). In particular, Fig. 4 is showing the details of the flowfield just upstream of the booster forward aerodynamic fairing. It should be emphasized that only velocity vectors corresponding to grid points in the central body mesh, in the cited plane, are represented in this figure. Velocity vectors associated with points in the booster grid were suppressed from the figure in order to

allow for a better visualization of the flowfield in the region. Flow deviation due to the booster is clearly seen in this figure. Furthermore, one can also clearly see in the figure the

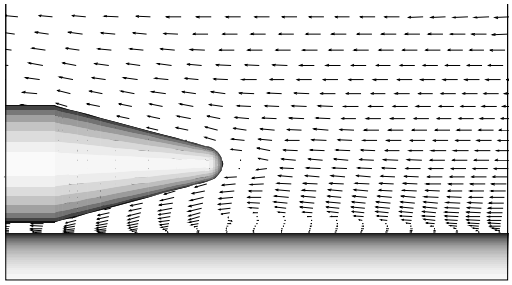

Figure 4: Detail of the velocity vector plot around the booster nose cap for laminar simulations with the coarse grid(M_∞ = 2, α = 0 deg., Re = 10 million).

recirculation region, which extends from approximately 2.5 booster diameters upstream of the booster nose until well within the conical booster section. The velocity profiles along a portion of this separation region seem to also indicate that there is even a secondary separation within the recirculation region. This last observation is corroborated by the streamline plot shown in Fig. 5. It must be emphasized, though, that Fig. 5 only shows a portion of the region depicted in Fig. 4 and, hence, it does not include the complete separation region.

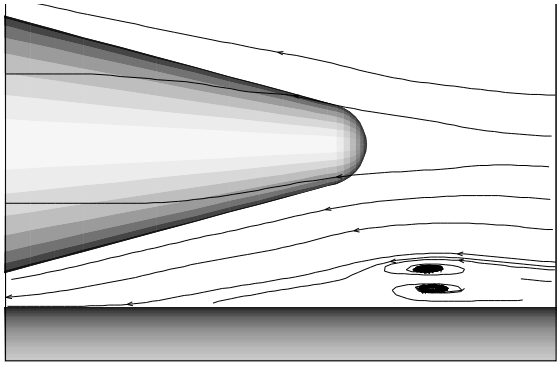

Figure 5: Streamlines near the booster nose for coarse grid laminar simulations (M_∞ = 2, α = 0 deg., Re = 10 million).

Pressure coefficient distributions on plane 1, along the vehicle central body wall, are shown in Fig. 6. Besides the comparison of the current laminar Navier-Stokes results and the experimental data, Fig. 6 also presents the pressure coefficient distribution obtained from the inviscid calculations reported in Ref. [1] for a similar grid. One can observe that, in the forward portion of the vehicle, the agreement between computational and experimental data is good.

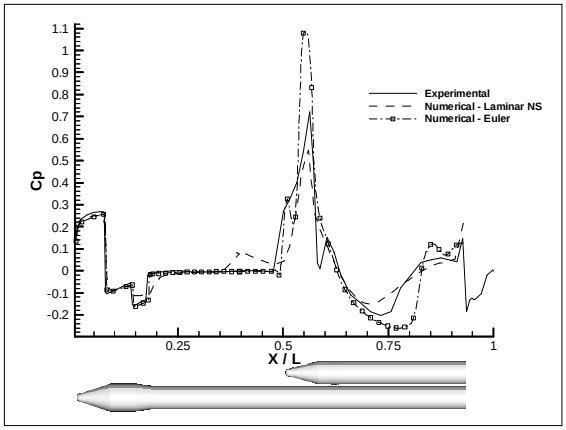

Figure 6: Pressure coefficient distributions for plane 1 along central body wall for coarse grid laminar simulations (M_∞ = 2, α = 0 deg., Re = 10 million).

There are discrepancies, however, in the boattail region. At the present time, the authors are not very much concerned about these differences in the boattail region because previous experience with axisymmetric calculations [11] has indicated that a very fine mesh is required to correctly capture the flow topology in this region. Essentially, at supersonic freestream conditions, there is an oblique shock impinging on the boattail-afterbody cylinder intersection. This shock interacts with the body boundary layer, creating a region in which fairly complex flow phenomena are present and, hence, a very fine grid in the longitudinal direction is required for accurately capturing the flow physics. Such a fine grid in the boattail region was not used in the present case because the computational resources available would not allow for the needed refinement in this region, and there was

an understanding that it would be more relevant, in the present case, to try to provide a better description of the region with strong interaction between central body and boosters. Therefore, the discrepancies observed in the boattail region could be resolved by the use of meshes as fine, in this region, as the ones described in Ref. [11]. Hence, it is a simple mesh refinement problem, which can be fixed in the future after the other problems are sorted out.

A sudden increase in the pressure coefficient distribution is observed at x/L ≅ 0.35 for the computational solution. The increase in Cp is due to the oblique shock wave create by the separation region along the central body. The experimental data do not have such pressure coefficient increase, clearly indicating that the experimental measurements do not see an oblique shock wave at this region in the flow. This could be explained by the fact that, at Re = 10 million, the flow is turbulent. A turbulent boundary layer does not have separate as easily due to an adverse pressure gradient as a laminar boundary layer. Hence, the flow separation upstream of the booster nose, which eventually is the originator of the oblique shock, can be simply a result of the treatment of the flow as laminar under conditions in which it is actually turbulent.

Further downstream, at x/L ≅ 0.50, the experimental measurements indicate a kink in the pressure coefficient distribution. This corresponds to the booster detached bow shock impingement on the central body. Clearly, the computational results do not display such effect due to the presence of the oblique shock wave upstream of the boosters. The position of the pressure peak at x/L ≅ 0.57 is correctly captured by the computation, although the magnitude of the pressure peak has a fairly significant error. There is a second pressure peak at x/L ≅ 0.61, which the computational results simply ignore. Downstream of this second pressure peak, there is a region with reasonably good agreement between experimental and computational data but, downstream of x/L ≅ 0.70, the discrepancies between computational and experimental results again become significant. One should observe, however, that the computational mesh used in these simulations corresponds to the coarse mesh used for the inviscid calculations reported in Ref. [1]. Hence, it is to be expected that mesh refinement should contribute to improvements in the correlation between computation and experiments.

A refined mesh was generated with 220 x 50 x 67 grid points for the central body mesh and 200 x 40 x 33 points for each of the booster meshes. As before, these numbers refer to grid points in the ξ, η and ς directions, respectively. This grid is referred to here as the fine grid. Moreover, this grid only contains half of the central body and two boosters, yielding a total of approximately 1.3 million grid points, which is pretty much in the upper limit for the computational resources available to the authors at the time. This grid implies in a factor of four increase in the azimuthal direction resolution of the central body grid and almost a factor of two increase in the longitudinal resolution of both central body and booster grids. Furthermore, since these launchers only fly at very low angles of attack, the consideration that the flow is symmetric about the pitching plane is not a severe restriction in the usefulness of the computations for design work. The same flight condition was considered for the simulations with the fine grid. Therefore, M_∞ = 2.0, the angle of attack is zero, Pr = 0.72, and the Reynolds number is 10 million, based on the diameter of the central body of the vehicle.

Figure 7 presents pressure contours on plane 1 (see Fig. 2) and along the surface of one of the boosters obtained with the fine grid. This figure only shows the flowfield around the nose cap of the boosters. In this case, the oblique shock wave upstream of the boosters, due to the flow separation previously described, is clearly evident in the figure. Moreover, the detached shock in front of the boosters and its interaction with the oblique shock are also clearly seen in the pressure contours. The impingement of the detached shock, from the booster that is out of the plane with regard to this visualization, on the booster on the upper part of the figure is also seen along the conical section of the latter

booster. Finally, the rapid flow expansion as it passes over the booster cone-cylinder intersection is also evident in Fig. 7. Hence, it is clear that the flow in this interaction region around the nose of the boosters is quite complex.

Pressure coefficient distributions along the central body, and on plane 1 (see Fig. 2), are shown in Fig. 8. As before, this figure compares experimental and viscous computational results, and it also includes the inviscid results reported in Ref. [1], for the same grid. It is clear that mesh refinement has improved the correlation between the results along the boattail region in the forward portion of the vehicle.

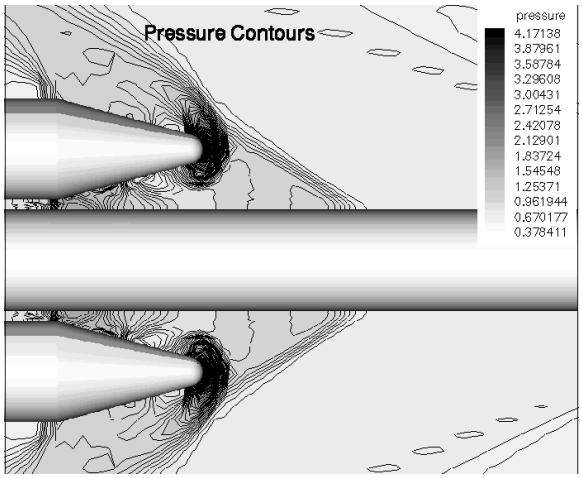

Figure 7: Dimensionless pressure contours along plane 1 and over the surface of one booster for fine grid laminar simulations (M_∞ = 2, α = 0 deg., Re = 10 million).

However, the agreement is still not perfect in this region but, as already discussed, the authors are not concerned about these discrepancies in the boattail region at the present time. The oblique shock wave due to flow separation ahead of the boosters is even more pronounced in this case, with a much better defined and stronger pressure jump at x/L ≅ 0.42. The position of the pressure peak at x/L ≅ 0.57 is again adequately captured by the calculation but, as before, the magnitude of the peak is still smaller than the experimental value. The difference in Cp peak magnitude is, however, smaller in this case than it was for the coarse grid results. Moreover, as one can clearly see in Fig. 8, the simulation starts to capture the second pressure peak at x/L ≅ 0.61. Furthermore, the agreement between experimental and computational Cp

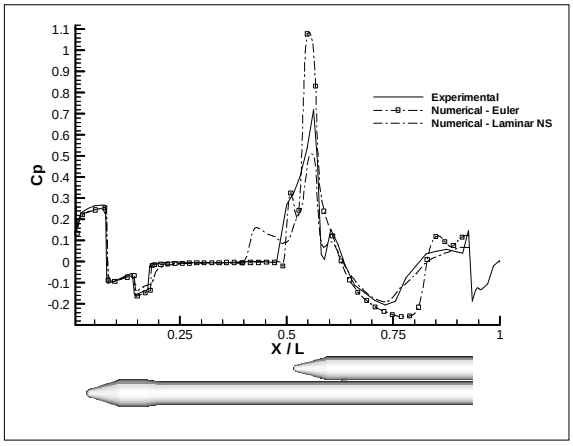

Figure 8: Pressure coefficient distributions for plane 1 along central body wall for fine grid laminar simulations (M_∞ = 2, α = 0 deg., Re = 10 million).

distributions downstream of this second pressure peak are remarkably good throughout the remaining of the vehicle. It must be emphasized that the present computations do not represent the vehicle nozzle region and, hence, it is not possible to match the results downstream of the x/L ≅ 0.92 station. A comparison of the Euler calculations discussed in Ref. [1] and the results in Fig. 8 indicate that the flow in the downstream sections of the vehicle include important viscous effects and there would be no way to obtain good agreement between experiments and computation without the inclusion of the viscous terms in the formulation.

3.2 Turbulents Viscous Simulations

For the flight conditions here considered, which essentially involve VLS flows with Reynolds numbers in the order to of 10^7 based on the body diameter, flowfields are clearly turbulent. Therefore, the implementation of turbulence models in the code is a necessary step in order

to provide an adequate representation of the flows of interest. The long term objective of this development work is to have a suite of models available in the code and let the user select the model that better suits his application. It is envisaged that, for the relevant flow conditions for the VLS, especially at angle of attack, a one-equation or a two-equation eddy viscosity model will be necessary for a correct representation of the flowfields. As an initial step towards this goal, a simple algebraic model has been implemented in the code so far. In particular, the algebraic Baldwin and Lomax [9] model is implemented in its standard form. This section describes some preliminary results obtained with this model.

The mesh used for the turbulent computations has 220 x 50 x 35 points, in the ξ, η and ς directions, respectively, for the central body grid and 180 x 40 x 33 points for each booster grid. As in the previous case, the pitch plane is assumed to be a symmetry plane in the flowfield and, hence, only half of the central body and two boosters are represented in the computational domain. The flight condition considered for these simulations is identical to the one considered in the previous cases. Moreover, here the turbulent Prandtl number was set to 0.9, which is consistent with other results reported in the literature. Figure 9 presents the Mach number contours for this simulation in the plane containing the axes of the central body and two boosters (plane 1 in Fig. 2). An observation of Fig. 9 indicates that the flowfield solution in this case is not much different from that obtained for the laminar calculations with the fine grid. In particular, one can clearly see the flow separation ahead of the boosters, along the central body, and the oblique shock wave which is formed upstream of this separation region. Actually, the flow separation region seems to be even larger in this case and it clearly extends further upstream than in the laminar calculations.

Figure 10 presents a comparison of pressure coefficient distributions along the central body for plane 1 (see Fig. 2). The curves shown in this figure include the experimental data, the turbulent computational results and the laminar computational results obtained with the fine mesh. It is evident from the figure that the separation occurs further upstream in the turbulent simulation when compared to the laminar solution.

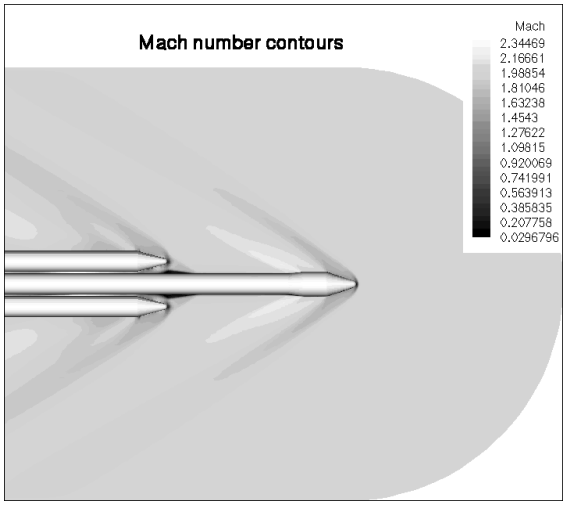

Figure 9: Mach number contours in the field (plane 1) for turbulent simulations (M_∞ = 2, α = 0 deg., Re = 10 million).

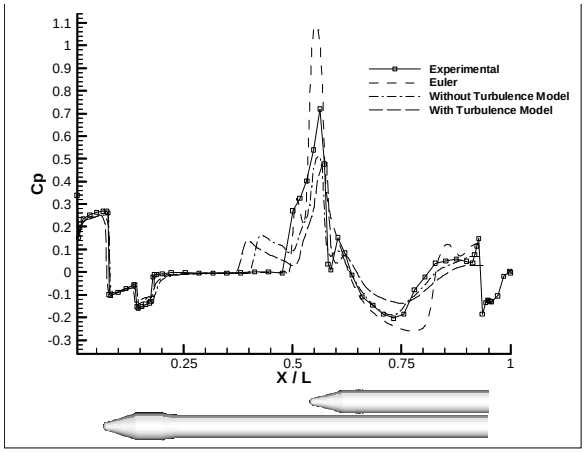

Figure 10: Comparison of pressure coefficient distributions along the central body wall for plane 1 (M_∞ = 2, α = 0 deg., Re = 10 million).

Furthermore, the agreement between computation and experiment, in the region downstream of the second pressure peak (x/L ≅ 0.61), is poorer for the turbulent simulations that it was for the laminar calculations on the fine grid. The two grids are not identical, but they

are sufficiently similar to rule out the possibility that the differences could only be credited to the grid. Finally, Fig. 11 presents the flow streamlines in the region around the booster nose cap for the turbulent simulation, and it shows details of the separated flow in this region. It is clear that the computations are indicating a fairly complex separated region, certainly including secondary separation within the original reversed flow bubble. It is, actually, quite questionable whether the Baldwin and Lomax model would be able to truly represent such a physically complex separated boundary layer, if the computational results were an accurate representation of the experimentally observed flowfield. The experimental pressure distributions, however, show no evidence of a separation region in this portion of the vehicle at this flight condition.

The initial expectation was that the implementation of a turbulence model could help improve the correlation between numerical and experimental data, in comparison with the type of agreement obtained in the previous section in which laminar computational results were reported. In particular, there was hope that the separation region upstream of the boosters would disappear and, hence, so would the

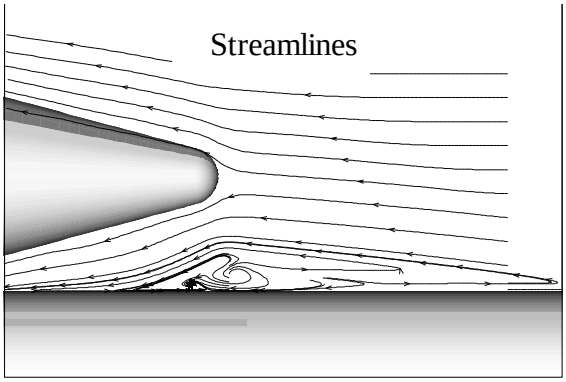

Figure 11: Detail of streamlines around the separation region for turbulent simulations (M_∞ = 2, α = 0 deg., Re = 10 million).

oblique shock wave, which is formed due to the separation. Clearly, this is not what the present results have shown. Furthermore, it is well known that the Baldwin and Lomax model has a tendency to add more eddy viscosity than what would actually be the correct amount to represent the correct physical behavior of the boundary layer. Hence, this means that the model has a tendency of stabilizing boundary layers that, actually, should separate. This compounds even further the questions with regard to the present turbulent simulations. The authors believe that, at the present time, the best that can be said with regard to the turbulent simulations is that their validation is still an ongoing process. At the time of this writing, different meshes are being generated for this problem and further analyses of the computational results are being performed. Fortunately, there are experimental results at different Reynolds numbers, for the same freestream Mach number, and these are being used in order to try to fully understand the discrepancies here observed. Furthermore, numerical parameters associated with the Baldwin and Lomax model are also being parametrically evaluated in order to fully explain the model behavior in this case.

4 Concluding Remarks

The paper describes viscous computations over the complete VLS vehicle. These calculations use a Chimera grid approach together with a finite difference numerical method to simulate supersonic flows over the complex VLS configuration including the central body and the strap-on boosters. Spatial discretization uses a central difference scheme plus added artificial dissipation terms. These are formed as a blend of second and fourth differences with an appropriate pressure switch, which detects the present of strong pressure gradients. Temporal discretization uses an explicit, 5-stage, 2nd-order accurate Runge-Kutta time stepping scheme with a spatially variable time step option for convergence acceleration for steady state problems. Algebraic grids are generated for each body of the complete configuration and these are coupled together in a Chimera sense in order to generate the complete composite grid for the overall configuration.

Despite the fact that Reynolds numbers of interest are of the order of 10^7, laminar calculation results are presented for two different meshes for the sake of code development and validation. The first mesh has approximately 830,000 grid points and it considers the complete vehicle, whereas the other has approximately 1.3 million grid points and treats the pitch plane as a symmetry plane. Results for the fine grid calculations show very good qualitative agreement with the experimental data for pressure coefficient distributions, except for the appearance of an oblique shock upstream of the booster nose cap region due to flow separation of the central body boundary layer. In particular, the quantitative agreement of the pressure coefficient distributions, between experiments and fine grid computational results, is very good and it demonstrates the need to include the viscous terms in order to correctly capture the phenomena present in the region of strong aerodynamic interaction between central body and boosters. Finally, some preliminary results for turbulent simulations using the Baldwin and Lomax algebraic eddy viscosity model are presented.

5 Acknowledgments

The present work was partially supported by Conselho Nacional de Desenvolvimento Científico e Tecnológico, CNPq, under the Integrated Project Research Grant No. 522.413/96-0. Additional support received from CNPq in terms of graduate scholarships for the first and second authors is also gratefully acknowledged. The authors are also indebted to Núcleo de Atendimento em Computação de Alto Desempenho, NACAD-COPPE/UFRJ, and to Centro Nacional de Supercomputação, CESUP/UFRGS, which have provided the computacional resources used for the present simulations.

6 References

[1] Basso, E., Antunes, A..P., and Azevedo, J.L.F., "Three Dimensional Flow Simulations Over a Complete Satellite Launcher With a Cluster Configuration," AIAA Paper No. 2000-4514, *Proceedings of the 18th AIAA Applied Aerodynamics Conference*, Vol. 2, Denver, CO, Aug. 2000, pp. 805-813.

[2] Wang, Z.J., and Yang, H.Q., "A Unified Conservative Zonal Interface Treatment for Arbitrarily Patched and Overlapped Grids," AIAA Paper No. 94-0320, 32nd AIAA Aerospace Sciences Meeting and Exhibit, Reno, NV, Jan. 1994.

[3] Wang, Z.J., Buning, P., and Benek, J., "Critical Evaluation of Conservative and Non-Conservative Interface Treatment for Chimera Grids," AIAA Paper No. 95-0077, 33rd AIAA Aerospace Sciences Meeting and Exhibit, Reno, NV, Jan. 1995.

[4] Jameson, A., Schmidt, W., and Turkel, E., "Numerical Solutions of the Euler Equations by Finite Volume Methods Using Runge-Kutta Time-Stepping Schemes," AIAA Paper No. 81-1259, June 1981.

[5] Turkel, E., and Vatsa, V.N., "Effect of Artificial Viscosity on Three-Dimensional Flow Solutions," *AIAA Journal*, Vol. 32, No. 1, Jan. 1994, pp. 39-45.

[6] Baldwin, B.S., and Lomax, H. L., "Thin Layer Approximation and Algebraic Model for Separated Turbulent Flows," AIAA Paper 78-257, Jan. 1978.

[7] Vieira, R., Azevedo, J.L.F., Fico, N.G.C.R., Jr., and Basso, E., "Three Dimensional Flow Simulation in the Test Section of a Slotted Transonic Wind Tunnel," ICAS Paper No. 98-R.3.11, *Proceeding of the 21st Congress of the International Council of the Aeronautical Sciences*, Melbourne, Australia, Sept. 1998 (publication in CD-ROM format without page numbering).

[8] Antunes, A.P., "Simulation of Aerodynamic Flows Using Overset Multiblock Meshes," Master Dissertation, Department of Aeronautical Engineering, Instituto Tecnológico de Aeronáutica, São José dos Campos, SP, Brazil, Aug. 2000 (in Portuguese, original title is "Simulação de Escoamentos Aerodinâmicos Utilizando Malhas de Blocos Múltiplos Sobrepostos").

[9] Pulliam, T.H., and Steger, J.L., "Implicit Finite-Difference Simulations of Three-Dimensional Compressible Flow," *AIAA Journal*, Vol. 18, No. 2, Feb. 1980, pp. 159-167.

[10] Swanson, R.C., and Radespiel, R., "Cell Centered and Cell Vertex Multigrid Schemes for the Navier-Stokes Equations," *AIAA Journal*, Vol. 29, No. 5, May 1991, pp. 697-703.

[11] Azevedo, J.L.F., and Buonomo, C.A., "Axisymmetric Turbulent Simulations of Launch Vehicle Forebody Flows," AIAA Paper No. 99-3528, 30th AIAA Fluid Dynamics Conference and Exhibit, Norfolk, VA, June-July 1999.